Spatial distribution and statistical properties of small-scale convective vortex-like motions in a quiet-Sun region

S. Vargas Domínguez,[1]★ J. Palacios,[2] L. Balmaceda,[3] I. Cabello[2] and V. Domingo[2]

[1]*Mullard Space Science Laboratory, University College London, Holmbury St Mary, Dorking, Surrey RH5 6NT*
[2]*Image Processing Laboratory, University of Valencia, PO Box 22085, E-46980 Paterna, Valencia, Spain*
[3]*Instituto de Ciencias Astronómicas, de la Tierra y del Espacio (ICATE), CONICET, Argentina*

ABSTRACT

High-resolution observations of a quiet-Sun internetwork region taken with the Solar 1-m Swedish Telescope in La Palma are analysed. We determine the location of small-scale vortex motions in the solar photospheric region by computing the horizontal proper motions of small-scale structures on time-series of images. These plasma convectively driven swirl motions are associated to (1) downdrafts (that have been commonly explained as corresponding to sites where the plasma is cooled down and hence returned to the interior below the visible photospheric level) and (2) horizontal velocity vectors converging on a central point. The sink cores are proved to be the final destination of passive floats tracing plasma flows towards the centre of each vortex. We establish the occurrence of these events to be 1.4×10^{-3} and 1.6×10^{-3} vortices Mm^{-2} min^{-1}, respectively, for the two time-series analysed here.

Key words: Sun: granulation – Sun: photosphere.

1 INTRODUCTION

The solar photospheric plasma is in constant evolution and is driven by convective processes in many spatial and temporal scales. Granular convective motions are of great interest as this process of energy exchange affects the evolution of magnetic structures while embedded in the plasma and might end up changing the topology of small emerging magnetic loops. By using high-resolution time-series at rapid cadences, we are nowadays able to register some of the finest and fastest scales of solar activity in an attempt to determine the Sun's structural building blocks. Investigations aim to describe the configuration and interactions of these features (i.e. magnetic concentrations) on their way up from the photosphere to upper layers in order to account for a more complete picture of solar activity.

The quiet Sun has proved to be more dynamic and magnetically active than previously thought (Domínguez Cerdeña, Kneer & Sánchez Almeida 2003), involving the rapid evolution of bright points (BPs) mostly associated to strong magnetic fields (up to the order of a few kG). Depending on their strength, magnetic concentrations are affected by the convective motions, being dragged and reconfigured through, for instance, fragmentation and coalescence phenomena (Viticchié et al. 2009). Moreover, small-scale and short-lived emerging magnetic loops represent a substantial part of the total magnetic flux (Martínez González & Bellot Rubio 2009) and therefore are useful to understand how they interact with the

photospheric plasma. It is also important to remark that granular convection has been proposed to be involved in the mechanism driving the production of an efficient turbulent dynamo responsible for the quiet-Sun magnetism (Petrovay & Szakaly 1993).

Vortical motions in the quiet photosphere associated to intense downdrafts are commonly found in theoretical simulations (Spruit, Nordlund & Title 1990; Zirker 1993; Stein & Nordlund 1998). Very recent simulations by Shelyag et al. (2011) have also shown that a large amount of vorticity in the photosphere is formed due to the interaction of plasma with the magnetic fields in the intergranular lane junctions. These types of vortex-like motions have been observationally reported at large spatial scales by Brandt et al. (1988), Title et al. (1992) and Attie, Innes & Potts (2009); at small scales by Bonet et al. (2008); and in the chromospheric quiet Sun by Wedemeyer-Böhm & Rouppe van der Voort (2009).

In this work, we concentrate on a quiet-Sun internetwork region that has been target of a few recent studies describing the presence of convectively driven vortex flows (Bonet et al. 2008, 2010), the coverage of BPs (Sánchez Almeida et al. 2010) and evidence of magnetic concentrations dragged by a swirl motion (Balmaceda et al. 2010). We use time-series of *G*-band images recorded at high cadence in order to compute the proper motions of structures in the observed region. By generating the horizontal velocity maps we discriminate the regions displaying a pattern of converging flows into a central point of intense strong downdrafts where the plasma is returned to the solar interior. These events are then tracked within the field-of-view (FOV). We estimate their lifetime to be around 10–20 min. Our results prove that the detected events cannot be

★E-mail: svd@mssl.ucl.ac.uk

considered as homogeneously distributed over the FOV. We high-
light the importance of understanding the effects of photospheric
vortical motions on the configuration of magnetic fields in their way
up to higher solar atmospheric layers, which are yet to be found.

2 OBSERVATIONS AND DATA PREPARATION

The data were acquired during a particular observing run on
2007 September 29 with the Swedish 1-m Solar Telescope (SST,
Scharmer et al. 2003) in La Palma, Canary Islands, as part of a long
international campaign with joint observations, making use of other
solar facilities at the Canary Islands Observatories. The region of
interest corresponds to a quiet-Sun area close to the solar disc centre
($\mu = 0.99$). Images in the G band ($\lambda = 430.56$ nm) were recorded at
a fast cadence, and the Multi-Frame Blind-Deconvolution (Löfdahl
2002) restoration technique was applied to correct the images from
the aberrations induced by the turbulent atmospheric medium that
affect their quality. The restored images with an effective FOV of
69×69 arcsec^2 and spatial sampling of 0.034 arcsec pixel^{-1} were
corrected with the standard procedures of flat-fielding, dark current
subtraction, and elimination of spurious pixels and borders, and
were grouped in two continuous time-series of images, *s1*: 08:47
to 09:07 UT and *s2*: 09:14 to 09:46 UT, with 15-s cadence. The
$\sim$7 min gap between series s1 and s2 corresponds to poor-quality
images due to bad observing conditions that had to be discarded.
The final steps included the compensation for diurnal field rotation,
destretching and subsonic filtering to eliminate residual jittering.
More details on the data preparation can be found in Balmaceda
et al. (2010).

3 SINKS AND CONVERGING FLOWS

Our analysis is based on the widely used local correlation tracking
techniques (LCTs, November & Simon 1988), implemented by
Molowny-Horas & Yi (1994). We compute the horizontal proper
motions of structures using a Gaussian tracking window with a full
width at half-maximum of 1.0 arcsec, to generate maps of horizontal
velocity (flow maps). The same procedure was used by Balmaceda
et al. (2010) on the same data for the analysis of a fraction of the
whole FOV (10×10 arcsec^2) displaying a region of strong negative
divergence. These authors found converging horizontal flows, that
is, the velocity arrows pointing to a common destination being the
location of the sink.

In this work, we present the results obtained from the LCT analy-
sis for series s1 and s2 over the complete FOV for 20-min intervals.
From the horizontal velocity maps, we compute the divergence field
defined as $\nabla \boldsymbol{v} = \frac{\partial \boldsymbol{v}_x}{\partial x} + \frac{\partial \boldsymbol{v}_y}{\partial y}$, where $\boldsymbol{v}_x$ and $\boldsymbol{v}_y$ are the corresponding
x- and y-components of the horizontal velocity vector.

Vertical velocities are inferred after multiplying the horizon-
tal flow divergence by the so-called scaleheight of the flux mass
($h_m = 150$ km), following November (1989). Note that the term
divergence refers to the divergence of the horizontal velocities. For
a detailed derivation, physical explanation and validity of this re-
lation, we refer the reader to Márquez, Sánchez Almeida & Bonet
(2006). Resulting vertical velocities are manifestly conditioned by
the LCT average and therefore cannot be directly compared to
Doppler velocities. An upcoming work attempts to establish mar-
gins for the comparison of the two. In our data, the velocity values
corresponding to a 20-min average range between 1.8 (upflows) and
-1.2 km s^{-1} (downflows). The overall distribution of horizontal ve-
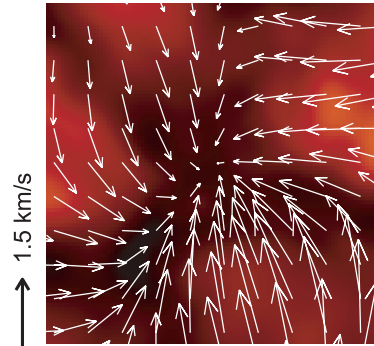locities of one of these events is shown in Fig. 1. There is a clear

Figure 1. Example of one of the detected events displaying horizontal
flows converging on a central point. The arrows represent the horizontal
velocity vectors inferred from the LCT. The displayed swirl motion exhibits
a counterclockwise sense of rotation. The background image represents the
20-min average image in false colour with a FOV of 3×3 arcsec^2.

trend in the direction of the velocity vectors, pointing towards the
centre of the image (*draining point*) and forming a swirl motion
with a counterclockwise sense of rotation. The background image
is the *G*-band intensity average over the 20-min interval. The centre
coincides with a dark structure formed by the junction of various
intergranular lanes.

Fig. 2 displays the vertical velocity maps for series s1 (upper
panel) and s2 (lower panel), using a common time-coverage of 20
min for both time-series (i.e. the total duration of series s1 and the
first 20 min of series s2) in order for the results to be comparable.
Regions showing intense upflows, denoted by different shades of
red colour, correspond to the intensive and recurrent activity from
exploding granules with velocities of $\sim$1 km s^{-1}, whereas strong
sinks with negative, that is, entering the plane of the figure, vertical
velocities of magnitude $\sim$0.9 km s^{-1} are observed as dark features.
The intergranular lanes are generally traced by the elongated struc-
tures in blue with downflows (-0.2 km s^{-1}). The black box in the
upper panel represents the FOV studied by Balmaceda et al. (2010).
Encircled in black are the locations of the detected vortical motions
(also referred to as events) from the horizontal flow pattern. The
selection was performed by visual inspection, considering a vor-
tex where velocity vectors in the flow map were converging and
changing the direction, defining a swirl. The area coverage of the
swirl events is assumed to be circular and drawn as the circles in
the maps, following the mentioned visual criteria. In all detected
cases, the events are located in regions with strong downflows (v_z
~ -0.8 km s^{-1}). Note that v_z represents the averaged v_{LOS} over
the time elapsed. The presence of all the events in at least two of
the consecutive flow maps over 5-min intervals suggests that they
remain coherent in a range between 10 and 20 min. The positions
of the events change from the first to the second time-series after
a 7-min gap in the observing run. (The dotted circles in the lower
panel in Fig. 2 show the location of the events in the upper panel
in the same figure for comparison.) These events do not seem to
be homogeneously distributed over the FOV but rather grouped in
certain locations resembling the mesogranular and supergranular
patterns.

Fig. 3 shows the final destination of passive tracers or *floats* (*white
dots* in the figure) driven by the computed mean field of horizon-
tal velocities, as commonly used to trace the evolution of plasma
motions (see, for instance, Yi 1992; Márquez et al. 2006). The back-
ground represents the averaged image in every case. The positions
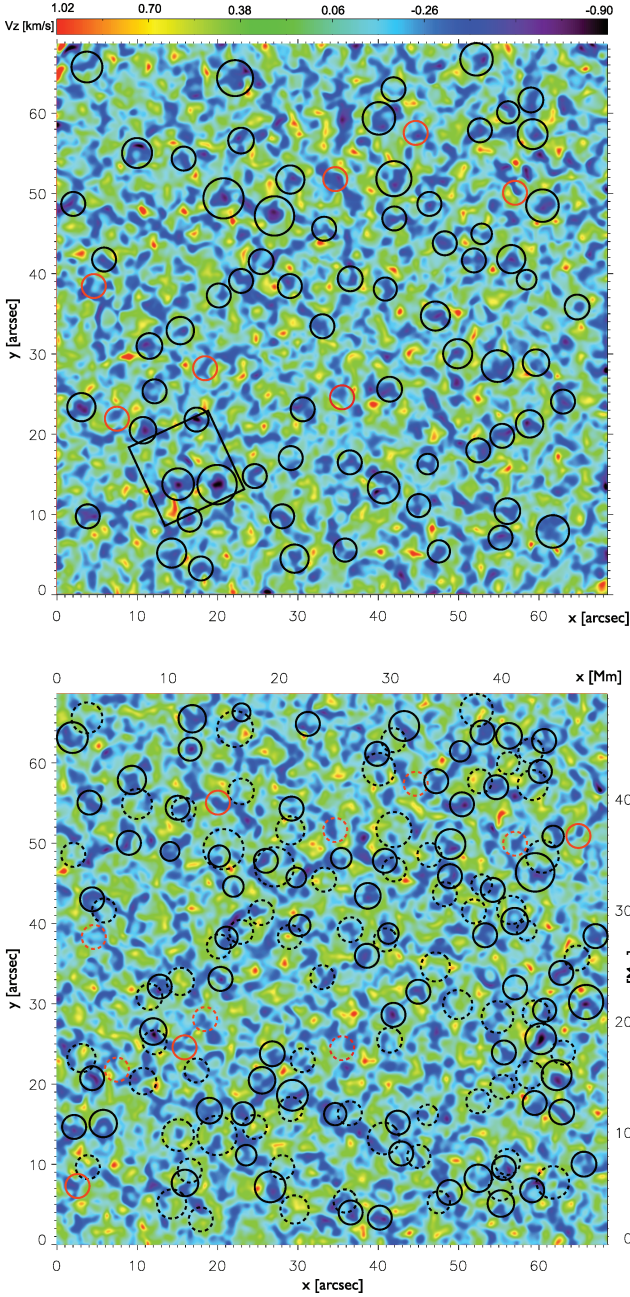of the events detected in Fig. 2 are this time encircled in blue/yellow

Figure 2. Maps of vertical velocities derived from the horizontal velocity field using LCT analysis for the SST/*G*-band time-series s1 (upper panel) and s2 (lower panel). The same time coverage of 20 min is used in both time-series. The black box represents the FOV analysed by Balmaceda et al. (2010), including a pair of strong swirl events. Encircled in black are regions in which the horizontal velocities are converging on a central point as inferred from the flow maps. The size of circles indicates the area coverage of the corresponding swirl event. The red circles denote peculiar regions with vertical velocities that do not conform to vortical flows. The dashed circumferences in the lower panel show the location of the events in the upper panel for comparison.

Figure 3. The images show the final destination of passive tracers (in white) driven by the computed mean field of horizontal velocities. The background represents the high-contrast image smoothed by the 20-min average in every case. Locations of the swirl events detected in Fig. 2 (black circles) are encircled in blue/yellow denoting the clockwise/counterclockwise sense of rotation. The red circles are regions in which there is a strong concentration of *floats*, also plotted in Fig. 2.

denoting the clockwise/counterclockwise sense of rotation. For both time-series, we found a larger number of counterclockwise motions, though the difference is not very significant. In general, these events are evidenced by a larger concentration of *floats* with the exception of a very few cases in the second time-series (lower panel) in which no sign of *floats* is detected though the areas are characterized by
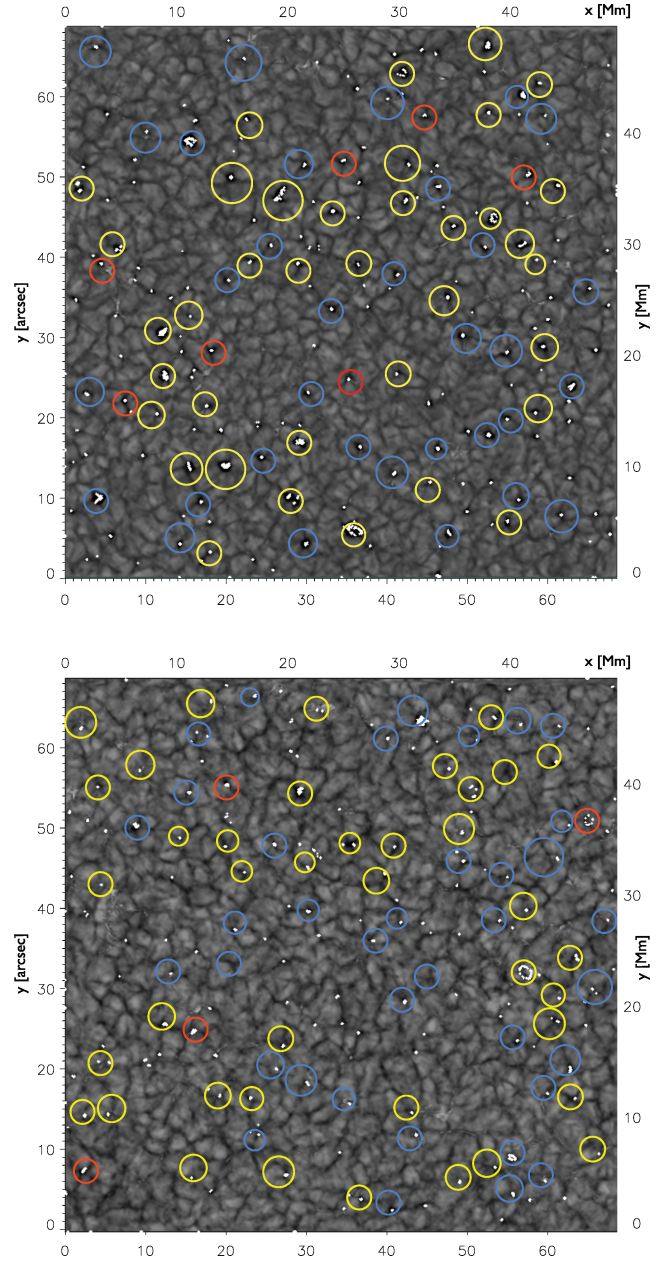
a junction of somewhat dark intergranular lanes. The distribution of vortices shows therefore a prominent correspondence with the location of intergranular lanes. The red circles in Fig. 3 are regions in which there is a strong concentration of *float* tracers, forming in some cases ring-shaped features. Although some of these regions display converging flows and correspond to downflows, they are not linked to very strong downflows when plotted over the image of vertical velocities (see the red circles in Fig. 2). Their location also changes from the first to the second time-series (e.g. compare the distribution of the red and red-dotted circles in the lower panel of Fig. 2). They do not represent though the most significant part

of the detected events but ∼10 per cent in both series. We have calculated the occurrence of the detected vortex-type events in the FOV, obtaining 1.46×10^{-2} and 1.09×10^{-2} vortices Mm^{-2} for the SST/*G*-band series s1 and s2, respectively (the values increase up to 1.66×10^{-2} and 1.25×10^{-2} vortices Mm^{-2} on including the events not associated to very strong downflows and encircled in red in Fig. 3.)

4 STATISTICS OF SWIRL MOTIONS

As discussed in the previous section, we have computed horizontal velocities and their corresponding divergences from *G*-band observations. With the location of the detected vortices (circles in Fig. 3), we define a binary mask used to compute some statistical properties in vortex-type areas (i.e. a mask of vortices). The vorticity is a vectorial magnitude whose direction is perpendicular to the *XY* plane. Using the equation $\nabla \times \boldsymbol{v} = \frac{\partial \boldsymbol{v}_y}{\partial x} - \frac{\partial \boldsymbol{v}_x}{\partial y}$, we compute vorticities of the horizontal flow, with v_z not included in the computation. Previous works have already studied vorticity in the solar photosphere using observational (Wang at al. 1995; Bonet et al. 2010) and theoretical (Stein & Nordlund 1998; Shelyag et al. 2011) approaches.

Fig. 4 (upper panels) shows histograms for the whole FOV of ∼ 50×50 Mm^2. Panel (a) displays independent results for series s1 (red) and s2 (blue), and total values for both series (black), resulting in a Maxwellian distribution of horizontal velocities, with a most probable value of 0.52 km s^{-1}. Histograms in panel (c) display a similar distribution of speeds using exclusively values within the mask of vortices. The most probable speed reduces to 0.48 km s^{-1}. Median values combining series s1 and s2, referred to as median$_{(s1+s2)}$, are shown in each panel in Fig. 4. Independent median values of the horizontal speed for series s1/s2 are 0.50/0.55 km s^{-1} in Fig. 4(a) and 0.51/0.44 km s^{-1} in Fig. 4(c). Large horizontal

velocities in the FOV are predominantly coming from recurrent exploding events (at the mesogranular scale) with large positive divergence values and hence the mean speed within vortex areas is expected to moderate as corresponding to negative divergences (convergences).

Same as with horizontal velocities and divergences, we have also plotted vorticity values over the whole FOV and in the mask of vortices (i.e. in the areas inside the circles in Figs 2 and 3). Figs 4(b) and (d) show the distribution of divergence (dashed lines) and vorticity (solid lines). Independent results are again plotted for series s1 (red) and s2 (blue), and total values for both series (black). When considering the total FOV, the divergence distribution is centred at a slightly negative value, indicating a preference for converging flows probably located at the edges of supergranular cells. This behaviour is more evident when considering vortex areas only (panel d). The vorticity distribution for the whole FOV shows a slight trend for the clockwise sense of rotation. Areas presenting vortices instead show a counterclockwise trend.

Fig. 5 plots a series of histograms computed using exclusively average values within the mask of vortices (i.e. mean values for each vortex). Vortices detected in series s1 and s2 show different vertical velocities vz, with more intense downflows observed in the latter. From the histograms in Fig. 5(a), most of the vortices are characterized by velocities of -0.4 and -0.6 km s^{-1} for series s1 and s2, respectively. It is important to bear in mind that vz is always negative since all vortices are observed in downflow areas, that is, areas where the divergence is negative, with vz being proportional to divergence times the scaleheight. Fig. 5(b) shows the distribution of the same quantities from Figs 4(a) and (c), but considering the mean values of speed in areas displaying vortices. The results are similar. In Figs 5(c) and (d), the distributions for
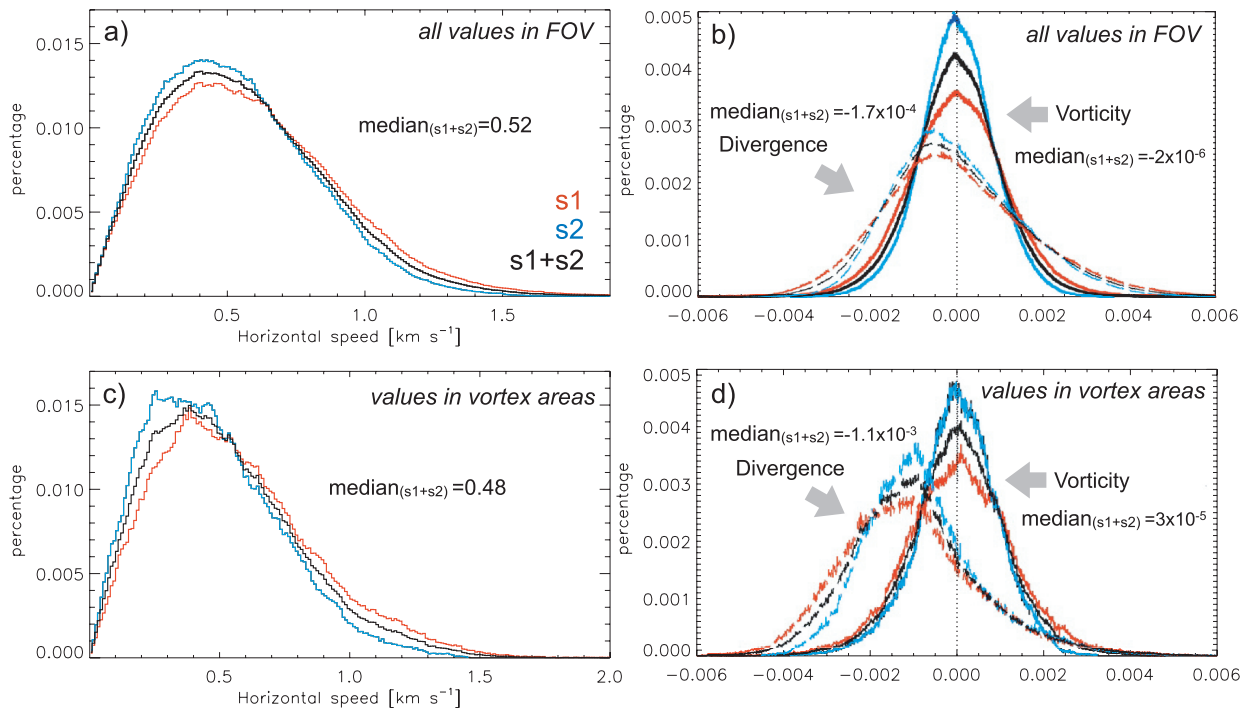

Figure 4. Panels (a) and (c): distribution of horizontal speeds. Panels (b) and (d): histograms of the values of divergence (dashed lines) and vorticity (solid lines). The upper panels plot values in all the FOVs, whereas the lower ones account for values within areas displaying vortices. All plots are computed using values for series s1 (in red), series s2 (in blue) and combined values for both time-series (in black). Corresponding most probable values for the combined case (s1+s2) are shown in the panels.
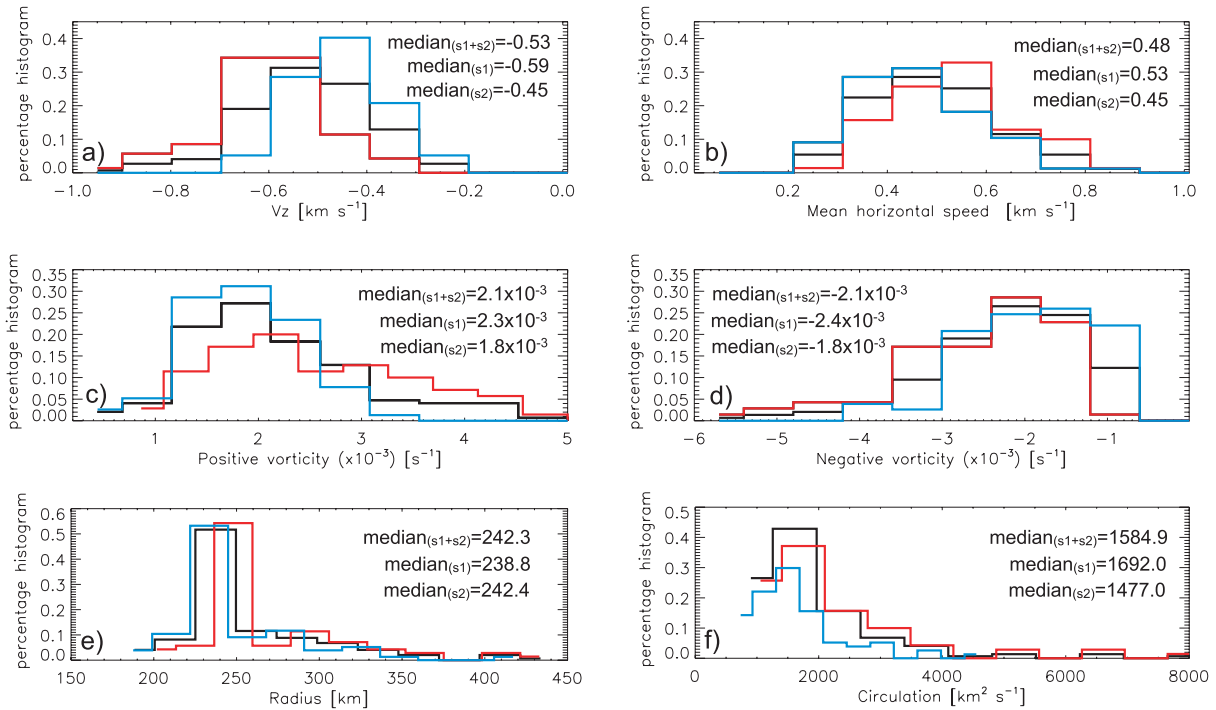
**Figure 5.** Histograms for data within the mask of vortices showing mean values of (a) vertical velocity, (b) horizontal speed, (c) positive vorticity, (d) negative vorticity, (e) radius of vortices, and (f) circulation, computed for the vortices in series s1 (in red), series s2 (in blue) and combined values for both time-series (in black). Corresponding most probable values for series s1 and s2, and for the combined case (s1+s2) are shown in the panels.
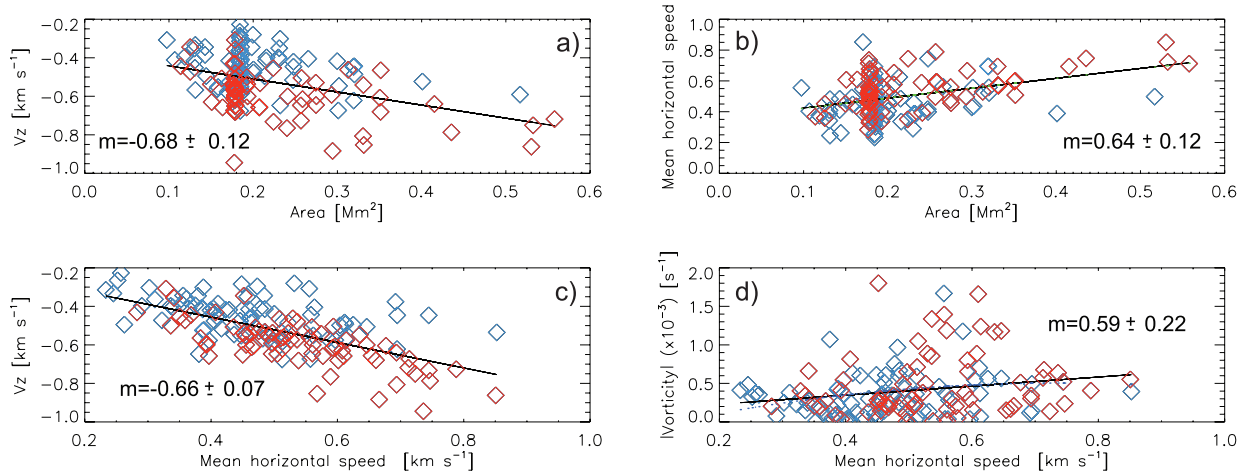
Figure 6. Scatter plots of properties characterizing the detected vortices. The diamonds represent the values for series s1 (red) and s2 (blue). The black lines are the result of linear fits applied over the data with their corresponding regression coefficients and errors shown.

positive and negative vorticities are shown. The medians for the counterclockwise and clockwise sense are comparable, indicating an apparent non-preferred sense of motion, though in Section 3 we found counterclockwise events as being slightly more numerous. Fig. 5(e) reveals a strong peak in the values between 240 and 250 km for the mean radius. It is worth noting the small size of the vortices that remain stable during the two series, since we would expect larger sizes, that is, of mesogranular scales, considering the 20-min average used for the LCT computation. In Fig. 5(f), we include the circulation, defined for each vortex as the mean absolute vorticity times their corresponding area. A peak value of 1584.9 km² s⁻¹ is clearly enhanced in the plots.

Fig. 6 displays scatter plots comparing different properties that characterize the vortices for series s1 (blue) and s2 (red). Linear fits are shown in black for the combined values of both series. For all panels, regressions were also separately computed for each series (not shown in the plots) with the resulting fits matching well between the two series. Panels (a) and (b) show the dependence of the vortex area and its corresponding velocities: larger vortices present higher horizontal and vertical speeds. This behaviour is also clear in panel (c). Larger scattering is observed in panel (d), where the dependence of mean horizontal speeds with vorticities is shown. However, the linear fit shows a trend of slightly higher vorticities for larger speeds.

5 DISCUSSION

Recent advances in solar instrumentations from ground-based and satellite telescopes are providing us with unprecedented high-resolution data, allowing for the study of the dynamics of the finest solar structures. The evolution of the solar granulation pattern at the photospheric level is of great interest due to the interaction between plasma and magnetic concentrations. In this scenario, vortices, formed in junctions of multiple intergranular lanes, are places in which the concentration of these magnetic features is expected to be favoured and therefore plays an important role in the dynamics of the quiet Sun (Kitiashvili et al. 2010).

We search for the location of small-scale swirls by tracking plasma motions in the same region where Bonet et al. (2008) detected small whirlpools by following the trajectories of BPs being swallowed by them. From 20-min average flow maps, we identify events displaying a converging pattern of horizontal velocity vectors towards a central point that correspond to the strong sinks as initially predicted by the numerical simulations. These events are in all cases detected in the junctions of multiple granules along very intense intergranular dark lanes. This is clearly seen on the average image for the duration of the time-series where the low-intensity junctions are enhanced (in Fig. 3). Data from the two time-series and a common examination allow the comparison of results. A total of 70 (in s1) and 77 (in s2) vortices have been detected, resulting in a density of 2.8×10^{-2} and 3.1×10^{-2} vortices Mm^{-2} for series s1 and s2, respectively.

Averaging over the 20-min window, we obtained space–time density values of 1.4×10^{-3} and 1.6×10^{-3} vortices Mm^{-2} min^{-1} for series s1 and s2, respectively. Values are comparable to the number obtained by Bonet et al. (2008) of 1.8×10^{-3} vortices Mm^{-2} min^{-1} and lower than the space–time density value of 3.1×10^{-3} vortices Mm^{-2} min^{-1} found by Bonet et al. (2010). It is necessary to bear in mind that the results from our flow fields are smoothed by the 20-min averages and the size of the employed tracking window. Many short-living vortical motions are likely diluted by the LCT temporal average.

BPs are distributed all over the FOV in this region as found by Sánchez Almeida et al. (2010) from which some describe spiral trajectories whilst being engulfed by downdrafts that Bonet et al. (2008) described as convectively driven vortex flows. We have compared the location of our detected vortices with the events discovered by Bonet et al. (2008) in the same solar region. As a result, we have found 68 per cent of coincidence, but the remaining 32 per cent corresponds to cases in the near vicinity of our vortices (i.e. less than 2 arcsec from the edge of the circular area enclosing the events in Figs 2 and 3.

We find for series s1 and s2 the counterclockwise/clockwise sense of rotation frequency value ratios of 53/47 and 52/48 per cent, respectively, which in view of the number of studied events show no significant difference with equally probable sense of rotation, in agreement with Bonet et al. (2008), though Bonet et al. (2010) find a significant preference in favour of the counterclockwise sense of rotation. The latter explain the different results, assuming that the vortex rotation is influenced by the latitudinal solar differential rotation, as the observations in Bonet et al. (2010) were done at mid-solar latitude, while the observations in Bonet et al. (2008) and, of course, in this paper, were carried out at the equator, where the influence of differential rotation is negligible.

In terms of dimensions, our detected vortices coincide with the values in Bonet et al. (2010) of less than 500 km in radius. The majority of our detected vortices exhibit a radius of 241 ± 25 km.

Some vortices, however, have a radius over 400 km that might not correspond to the main vortical scale detected but to signatures of larger scales of vortical motions. For the circulation, we also found a pronounced peak value, at 1585 km^2 s^{-1}. This value is nearly half of 4000 km^2 s^{-1} for the vortex presented by Brandt et al. (1988) which covers an area of about 5 granules and hence corresponds to a much larger mesogranular scale.

Strong interacting vortices may play a role in the excitation of solar acoustic oscillations, as shown by Kitiashvili et al. (2010). In particular, these authors propose that high-speed vortices can attract and capture other vortices with opposite sense of rotation and their interaction might lead to their partial annihilation. In our sample of vortices, we find several examples with these characteristics, though a deep analysis of the interaction of opposite-sign vorticities is out of the scope of this work.

More observational evidence from spectropolarimetric data would be required to complete the analysis and determine up to what extent the magnetic concentrations in the nearest vicinity of the detected swirl events are affected by the appearance of the vortex. An example of magnetic features appearing as being dragged by this type of convective motions was presented by Balmaceda et al. (2010) in one of the vortices within the FOV. This type of vortical convective flows are thought to contribute to gathering magnetic fragments, thus amplifying weak magnetic fields near the surface and representing an important mechanism for the formation of more stable features (Danilovic, Schüssler & Solanki 2010). Exhaustive analysis of the intensification of the magnetic field in vortex-like regions and its morphology at different solar atmospheric layers will also contribute with precise inputs to advance numerical simulation development.

REFERENCES

Attie R., Innes D. E., Potts H. E., 2009, A&A, 493, L13
Balmaceda L., Vargas Domínguez S., Palacios J., Cabello I., Domingo V., 2010, A&A, 513, L6
Bonet J. A., Márquez I., Sánchez Almeida J., Cabello I., Domingo V., 2008, ApJ, 687, L131
Bonet J. A. et al., 2010, ApJ, 723, L139
Brandt P. N., Scharmer G. B., Ferguson S., Shine R.A, Tarbell T. D., 1988, Nat, 335, 238
Danilovic S., Schüssler M., Solanki S. K., 2010, A&A, 509, A76
Domínguez Cerdeña I., Kneer F., Sánchez Almeida J., 2003, ApJ, 582, L55

Kitiashvili I. N., Kosovichev A. G., Wray A. A., Mansour N. N., 2010, ApJ, 719, 307

Löfdahl M. G., 2002, in Bones P. J., Fiddy M. A., Millane R. P., eds, Proc. SPIE Vol. 4792, Image Reconstruction from Incomplete Data. SPIE, Bellingham, p. 146

Márquez I., Sánchez Almeida J., Bonet J. A., 2006, ApJ, 638, 553

Martínez González M. J., Bellot Rubio L. R., 2009, ApJ, 700, 1391

Molowny-Horas R., Yi Z., 1994, ITA, Internal Rep. No. 31

November L. J., 1989, ApJ, 344, 494

November L. J., Simon G. W., 1988, ApJ, 333, 427

Petrovay K., Szakaly G., 1993, A&A, 274, 543

Sánchez Almeida J., Bonet J. A., Viticchié B., Del Moro D., 2010, ApJ, 715, L26

Scharmer G. B., Bjelksjö K., Korhonen T. K., Lindberg B., Petterson B., 2003, in Keil S. L., Avakyan S. V., eds, Proc. SPIE Vol. 4853, Innovative Telescopes and Instrumentation for Solar Astrophysics. SPIE, Bellingham, p. 341

Shelyag S., Keys P., Mathioudakis M., Keenan F. P., 2011, A&A, 526, 5

Spruit H. C., Nordlund A., Title A. M., 1990, ARA&A, 28, 263

Stein R. F., Nordlund A., 1998, ApJ, 499, 914

Title A. M., Topka K. P., Tarbell T. D., Schmidt W., Balke C., Scharmer G., 1992, ApJ, 393, 782

Viticchié B., DelMoro D., Berrilli F., Bellot Rubio L. R., Tritschler A., 2009, ApJ, 700, L145

Wang Y., Noyes R. W., Tarbell T.d., Title A. M., 1995, ApJ, 447, 419

Wedemeyer-Böhm S., Rouppe van der Voort L., 2009, A&A, 507, L9

Yi Z., 1992. PhD thesis, Univ. Oslo

Zirker J. B., 1993, Sol. Phys., 147, 47

This paper has been typeset from a TEX/LATEX file prepared by the author.